

Quantum Dynamical Signatures of Topological Flow Transitions in Limit Cycle Phases

Alejandro S. Gómez¹ and Javier del Pino¹

¹Departamento de Física Teórica de la Materia Condensada and Condensed Matter Physics Center (IFIMAC), Universidad Autónoma de Madrid, E-28049 Madrid, Spain

Quantum self-oscillatory phases are ubiquitous in driven-dissipative systems. Classically, each phase is defined by its flow pattern and how stationary sets organize phase space (e.g. fixed points and limit cycles), with transitions triggered by local bifurcations or global basin rearrangements. In the quantum regime, these reorganizations are often blurred by density-matrix averaging, and spectral indicators such as the Liouvillian gap can miss changes that unfold mainly in the transients. Here we introduce a topological graph invariant, the molecule, which captures the phase-space connectivity of fixed points and limit cycles. Transitions show up as discrete changes of this invariant, with each form marking a distinct quantum dynamical pattern (e.g. relaxation pathway). The molecule encodes the global topological constraints that govern how stationary sets and their basins can rearrange, clarifies when such rearrangements can affect the Liouvillian modes, and reveals additional transitions that remain hidden in the steady-state spectrum but stem from global changes of the flow topology. Our findings show that flow topology offers a clear and unified way to identify and classify dynamical phases beyond what Liouvillian spectra alone reveal.

Introduction: Driven-dissipative quantum systems provide a rich arena to explore non-equilibrium dynamical phases of matter. Of particular interest are self-oscillatory states, where the system sustains oscillations at frequencies distinct from the drive. They appear as subharmonic responses (e.g., period-doubling in parametrically driven resonators) [1–4] and as limit cycles (LCs), isolated orbits in phase space with spontaneous oscillation frequencies set by the balance of nonlinearity, dissipation, and coherent drive [5–11]. Driven-dissipative phases arise naturally in quantum platforms engineering parametric amplification and strong nonlinear interactions, such as superconducting, cold atoms, trapped ions, and nanomechanical systems [12–15]. Moreover, leveraging such states is key to quantum control [16], generating frequency combs [17], stabilizing error-correction codes [18], and realizing collective many-body phases [19–21].

Self-oscillations appear stationary in a suitable rotating frame, allowing dynamical phases to be classified using intuition from time-independent systems [22]. In this picture, phase transitions occur when a quasienergy gap of the Floquet Hamiltonian closes [23]. In open driven systems, the same logic applies to the Liouvillian, which evolves the density matrix: closing the real part of its spectrum marks a dissipative transition, while closing its complex (non-Hermitian) gap can reorganize the oscillatory modes of the system [24, 25]. However, these spectral indicators are insufficient to determine the specific dynamical change because the density matrix averages over phase space. This averaging specifically prevents distinguishing between a local versus a global reorganization in phase space. This limitation is critical in regimes like parametric instabilities or superradiant transitions, which generate coexisting multi-modal self-oscillatory responses (e.g., period-doubling and LCs). [26–28].

In the large-excitation limit, the dynamics reduce to a phase-space flow organizing all deterministic trajectories.

Each distinct flow pattern then defines a *phase*, whose long-term behavior is set by its attractors, typically fixed points (FPs) or LCs. In 2D (Morse) flows containing only FPs, a graph invariant captures their persistent qualitative pattern under small parameter changes. [29] In driven-dissipative systems, FP attractors also carry a symplectic norm distinguishing particle- and hole-like behavior [22, 30–32], which must enter the invariant [33]. The invariant changes only when the flow undergoes reorganizations, from local shifts in FP stability or symplectic norm to global bifurcations away from FPs. The symplectic norm flip can be directly read from the linear response [22, 34, 35]. But once LCs enter, reorganizations of LCs and FPs become intertwined, making the FP invariant incomplete. For instance, LCs set extended phase-space boundaries that constrain local changes and also undergo their own global events, such as saddle-loops or LC-LC collisions. [36, 37] A key question follows: how do we build an invariant that incorporates both FPs and LCs, captures their global transitions, and predicts their physical signatures?

In this work, we introduce a topological framework for self-oscillating driven-dissipative phases. Guided by the classification of *structurally stable* (qualitatively robust) flows with LCs, called Morse-Smale flows [29], we define a *molecule*, an invariant encoding the arrangement and chirality of FPs and LCs on equal footing, with FP chirality set by the symplectic norm in the high-excitation limit. The molecule condenses the full deterministic phase-space dynamics into a single visual object. Its structure, set by the orientation and ordering of neighboring flow regions, dictates how the invariant can change at bifurcations and thus which phase transitions are topologically allowed or forbidden. Because the flow provides the scaffold for the quantum dynamics, these transitions imprint clear signatures in transient quantum states, even though they need not clearly manifest in the Liouvillian spectrum. As an illustration, we apply the framework to a parametri-

cally driven Kerr resonator with nonlinear loss and gain, a model capturing the core mechanisms of self-oscillatory phases across quantum platforms such as trapped ions, levitated systems, light-matter ensembles, superconducting circuits, and hybrid quantum devices.

Reference model: Our model consists of a nonlinear Kerr parametric oscillator of natural frequency ω_0 , with annihilation operator \hat{a} driven near parametric resonance at frequency 2ω and subject to linear gain and nonlinear loss [Fig. 1(a)]. In the lab frame, the system is invariant under discrete time translations $t \mapsto t + nT$ by multiples of its drive period $T = 2\pi/\omega$. Moving to a rotating frame at frequency ω (doubled period $2T$) and applying the rotating-wave approximation, the density matrix evolves as $d\hat{\rho}/dt = \mathcal{L}[\hat{\rho}; \boldsymbol{\eta}]$ with time-independent Liouvillian

$$\mathcal{L}[\square; \boldsymbol{\eta}] = -i[\hat{\mathcal{H}}, \square] + \sum_i [c_i \square c_i^\dagger - \frac{1}{2}\{c_i^\dagger c_i, \square\}], \quad (1)$$

where Hamiltonian $\hat{\mathcal{H}}$ and collapse operators \hat{c}_i read,

$$\hat{\mathcal{H}} = -\Delta \hat{a}^\dagger \hat{a} + \frac{U}{2} \hat{a}^\dagger \hat{a}^2 + \frac{G}{2} (\hat{a}^\dagger \hat{a}^2 + \hat{a}^2), \quad (2)$$

$$\hat{c}_i \in \{\sqrt{\kappa_-} \hat{a}, \sqrt{\kappa_+} \hat{a}^\dagger, \sqrt{\kappa_2} \hat{a}^2\}. \quad (3)$$

The vector $\boldsymbol{\eta} = (\Delta, U, G, \kappa_-, \kappa_+, \kappa_2)$ collects all parameters entering the right-hand side of Eq. (1). Here $\Delta = (\omega^2 - \omega_0^2)/\omega$ is a detuning from parametric resonance, U is the Kerr nonlinearity, G the two-photon drive amplitude. The collapse operators account for single-photon loss (rate κ_-), single-photon gain (rate κ_+), and two-photon loss (rate κ_2) respectively.

The model in Eq. (1) and Eq. (2) descends from the Mathieu-Van der Pol-Duffing oscillator [39] after moving to a rotating frame and applying the rotating-wave approximation around $\omega_0 \approx \omega$ [8]. It interpolates between several standard nonlinear oscillators: it becomes the Kerr parametric oscillator (KPO) for $\kappa_2 = 0$ [40], the two-photon-dissipative parametric oscillator (2DPO) for $U = 0$ and $\kappa_2 > 0$ [41], and the Rayleigh-Van der Pol oscillator (RVdP) for $G = 0$ and $\kappa_+ > 0$ [8]. A common approach to dynamical phase transitions is to track the Liouvillian spectrum as $\boldsymbol{\eta}$ varies. The steady state $\hat{\rho}_0$ corresponds to the eigenmode with vanishing decay rate, i.e., with Liouvillian eigenvalue λ_0 such that $\text{Re}\{\lambda_0\} = 0$. In Fig. 1(b) we show the Wigner function of $\hat{\rho}_0$ in several illustrative limits, giving a phase-space picture of the quantum state; Fig. 1(c) displays the corresponding Liouvillian spectra. In the KPO and 2DPO limits, the Wigner function is bimodal, corresponding to a coherent-state mixture with $\text{Im}\{\lambda_0\} = 0$, rotating in the lab frame at frequency ω . In the RVdP steady state, probability concentrates along a closed orbit that corresponds to a LC. Time-translation symmetry is continuously broken, as the system oscillates with an emerging frequency ω^* , which appears as a conjugate pair of Liouvillian eigenvalues $\text{Im}\{\lambda_{0,\pm}\} = \pm\omega^*$. In the classical limit, the periodic

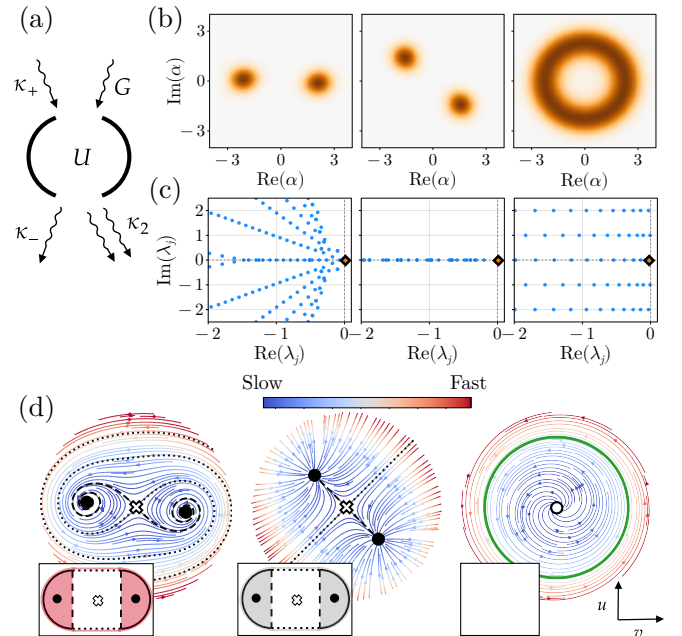


FIG. 1. *Flow topology of driven-dissipative nonlinear resonators* (a) Driven-dissipative resonator with Kerr nonlinearity U , two-photon drive G , single- and two-photon loss κ_- , κ_2 , and single-photon gain κ_+ . (b) Steady-state Wigner function for a Kerr Parametric Oscillator (KPO, $\kappa_2 = 0 = \kappa_+$, $U = -0.1$, $G = 0.25$, $\Delta = 0$), a two-photon driven dissipative oscillator (2DPO, $U = 0 = \kappa_+$, $G = 0.25$, $\kappa_2 = 0.1$, $\Delta = 0$), and a Rayleigh Van der Pol oscillator (RVdP, $\kappa_2 = 0.01$, $\kappa_+ = 0.1$, $U = -0.1$, $\kappa_- = 0$, $G = 0$ and $\Delta = 1$). For the KPO and 2DPO cases, the single-photon loss is set to $\kappa_- = 0.1$. (c) Corresponding Liouvillian spectrum and (d) mean-field vector flows in the rotating quadratures (u, v) . FP attractors (repellors), LCs, and saddles appear as black (white) dots, green curves, and white crosses, respectively. Boxed insets show the flow-topology graph invariants built from the FPs and their separatrices [33]. Red (gray) shading marks regions of negative (zero) chirality in the basins of attraction of the corresponding FPs. A flow containing a LC falls outside the classification.

motion produces an infinite Liouvillian ladder at all LC harmonics, $\text{Im}\{\lambda_{0,n}\} = \pm n\omega^*$. At low photon numbers, this ladder smoothly deforms into parabolic branches [42]. In all these phases the Wigner function remains positive, indicating that $\hat{\rho}_0$ admits a classical phase-space description, even though the transient evolution can generate Wigner negativity, a hallmark of nonclassical states.

Flow-topology classification: We associate to $\mathcal{L}[\hat{\rho}; \boldsymbol{\eta}]$ a planar flow $dr/dt = \mathbf{f}(r, \boldsymbol{\eta})$ in the real quadratures $r = (u, v)^T$ defined by $\text{Tr}[\hat{\rho}\hat{a}] = u + iv$, via a mean-field factorization $\langle \square \Delta \rangle \simeq \langle \square \rangle \langle \Delta \rangle$, which neglects quantum correlations. From Eq. (1) and Eq. (2) we find

$$\mathbf{f}(r, \boldsymbol{\eta}) = \begin{pmatrix} \left(\frac{\gamma}{2} - \kappa_2 R^2\right) u - (\Delta + G - UR^2)v \\ \left(\frac{\gamma}{2} - \kappa_2 R^2\right) v + (\Delta - G - UR^2)u \end{pmatrix}, \quad (4)$$

where $R = \sqrt{u^2 + v^2}$ and $\gamma \equiv \kappa_+ - \kappa_-$. The flows corre-

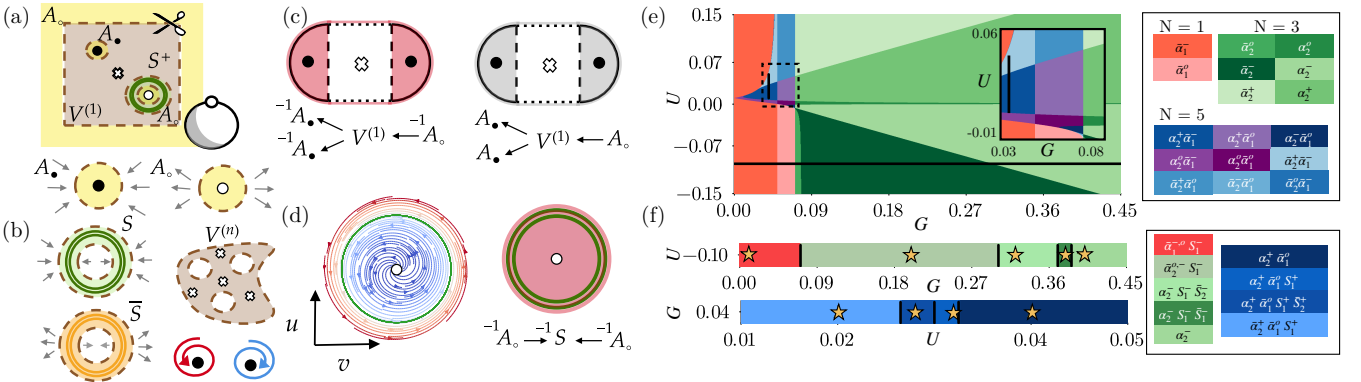


FIG. 2. *Fixed-point phase topology and Morse-Smale invariants in the (U, G) plane.* (a) Cutting-set construction used to compactify the flow; the white dot represents the source at infinity. (b) Elementary atoms and chirality convention: FP attractor A_\bullet , repellor A_\circ , attracting/repelling LC S, \bar{S} , and saddle region $V^{(n)}$. (c) Morse-Smale graphs for the KPO and 2DPO of Fig. 1(d) and associated molecules. (d) Example of graph invariant, similar to [33], and molecule built by these rules for a RVdP flow with an attracting LC. (e) Phase diagram versus (U, G) with legend of FP classes, inset zooms the dashed region. The labelling of the phases is detailed in the main text. Parameters fixed (a.u.): $\Delta = 0.05$, $\kappa_+ - \kappa_- = 0.1$, $\kappa_2 = 0.01$. (f) One dimensional cuts at $U = -0.10$ and $G = 0.04$ from (e), showing the number of attracting (repelling) LCs in each region $S_k^i (\bar{S}_k^i)$; stars mark the (U, G) points for the flows in Figs. 3. For further details on the marked flows, see [38].

sponding to the parameter values of Fig. 1(b) are shown in Fig. 1(d). Their stationary sets ($t \rightarrow \infty$) consist of FPs (solutions to $\mathbf{f} = 0$) of attractor, repellor or saddle type, depending on the stability, and LCs (closed isolated trajectories $\mathbf{r}^*(t + T^*) = \mathbf{r}^*(t)$ fulfilling Eq. (4)), which act as periodic attractors or repellors. The flow also contains separatrices, trajectories that mark the boundaries between regions whose initial conditions evolve toward different long-term behaviors (basins of attraction). Bifurcations mark abrupt reorganizations of the flow. They may be *local*, creating or destroying FPs across instabilities, or *global*, such as separatrix reconnections and reshaping of entire basins without changing the set of FPs. Figures 1(b),(d) show that in the semiclassical regime, the steady state $\hat{\rho}_0$ inherits the structure of the phase-space flow (4): the flow determines how weak quantum fluctuations circulate around and between attracting FPs and LCs, which accumulate probability in their basins. In the strongly fluctuating regime this correspondence can break down, as noise or quantum jumps can “wash out” the classical structure [35]. This prompts the question of whether the flow can track transient quantum dynamics with LCs more directly than the Liouvillian spectrum and better expose the underlying dynamical phases.

A natural way to address this question is to collect the essential structure of the flow (FPs, LCs, and separatrices), and use this to define a topological invariant. For generic parameters η , the flow (4) is structurally stable and satisfies the Morse–Smale conditions [38] (it has finitely many FPs and LCs, and it does not contain saddle connections). The flow thus admits a combinatorial, topological invariant. In systems combining Hamiltonian dynamics with dissipation, FP attractors with different local chiralities are physically distinct: chirality sets the

symplectic norm (particle-hole character) of local fluctuations, determining whether they behave as excitations of a locally harmonic or inverted oscillator [22, 34]. In the absence of LCs, a complete invariant that incorporates this local chirality forms a decorated graph [33].

Inspired by Morse-Smale flow classification [29], we extend this framework to include LCs by condensing the flow’s topological structure into an object dubbed *molecule*: Its vertices, or *atoms*, represent local attractors (dubbed A_\bullet), repellors (A_\circ), attracting or repelling LCs (S and \bar{S}) and the regions with n saddles $V^{(n)}$ [Fig. 2(a,b)]. Its edges trace the separatrices that connect them. Furthermore, the molecule encodes how the flow’s local orientations (chiralities), relate across the regions connected by separatrices. Two molecules are equivalent when their separatrix graphs match and chirality is preserved, meaning they describe the same phase; bifurcations break this equivalence and can be thus regarded as *phase transitions*. To build the molecule, we (i) compactify the flow in flat phase space into a sphere, in similar spirit to Ref. [33]. Next, (ii) we define a cutting set [Fig. 2(a,b)]: a disc around each A atom, an annulus around each S atom, and a small neighborhood around each $V^{(n)}$. Cutting along these boundaries separates the atoms, which become the nodes of the graph. Note that the elementary atom associated with the additional “virtual” source at infinity, A_\circ , must also be included. (iii) We then add the bonds of the molecule: directed edges of type s , t , or u for repellor-saddle, repellor-attractor, and saddle-attractor connections, following the time-forward flow. (iv) Finally, we assign chirality to the cutting set of each atom individually, extending the FP chirality marker of Ref. [33]: +1 for CW, -1 for CCW, and no label when chirality is undefined (overdamped ringdown). This chirality assignment

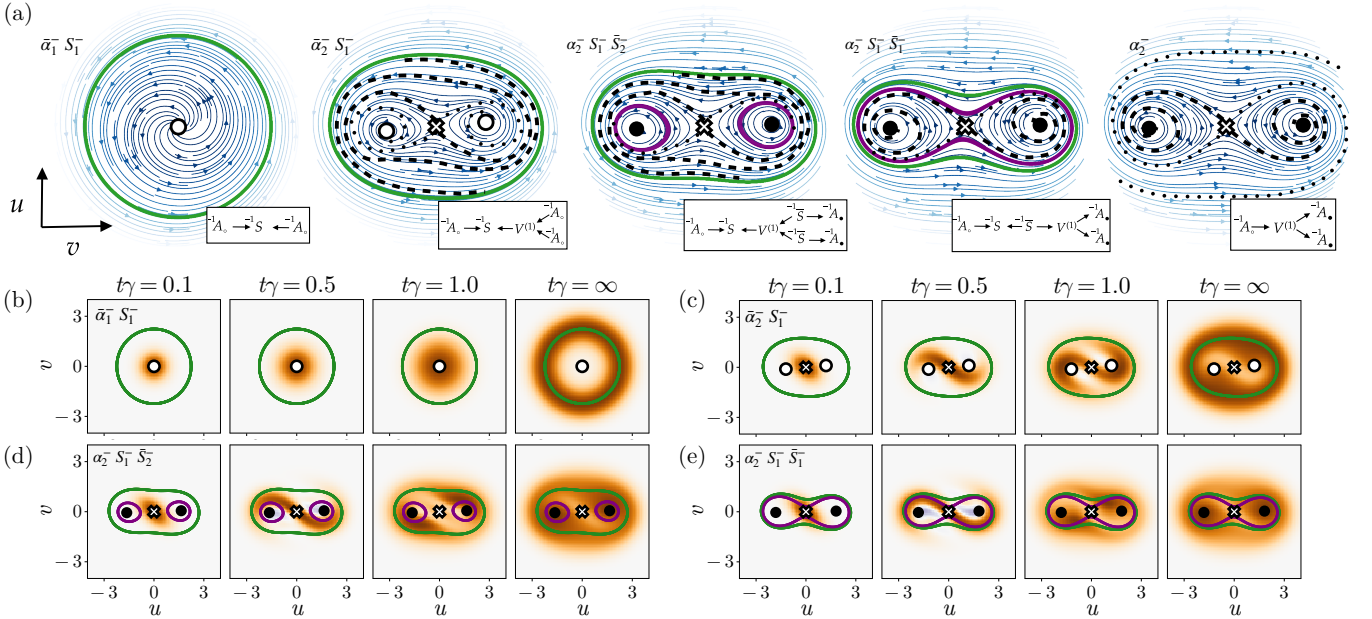


FIG. 3. *Flow topology and quantum evolution toward steady states.* (a) Semiclassical flows for starred points of Fig 2(f) with $G = 0.01, 0.20, 0.32, 0.38, 0.40$, (phases denoted $\bar{\alpha}_1^- S_1^-$, $\bar{\alpha}_2^- S_1^-$, $\bar{\alpha}_2^- S_1^- \bar{S}_2^-$ and $\bar{\alpha}_2^- S_1^- \bar{S}_1^-$) together with their topological invariants (molecules). Attracting (repelling) LCs are shown as green (purple) curves, and qualitative stable (unstable) separatrices as dashed (dotted) lines. (b-e) Wigner function at intermediate times (see panel titles) and in the steady state ($t \rightarrow \infty$).

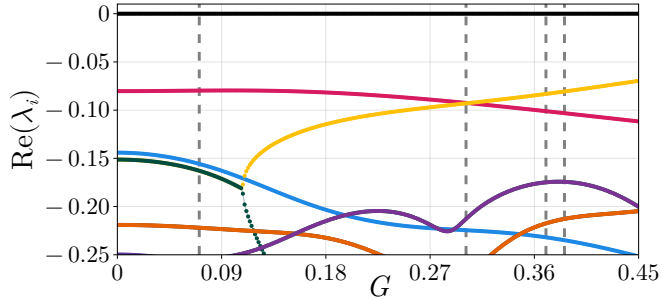


FIG. 4. *Liouvillian spectrum sensitivity to flow-topology transitions.* Real part of the low-lying Liouvillian eigenvalues $\text{Re}(\lambda_i)$ as a function of the amplitude driving G . The steady state corresponds to the eigenvalue $\lambda_0 = 0$ (black solid line). The vertical dashed lines denote the critical values associated with the local and global phase transitions identified in Fig. 2(f).

goes beyond the standard Morse-Smale scheme, where a global saddle orientation lets FPs rotate freely. Crucially, LCs require a finer notion of orientation and adjacency than FP flows because their inner and outer flows can carry different chiralities [29]. Additional details on the molecule construction can be found in [38].

Excluding LCs, the molecule reduces to an object akin to the FP graph invariants of Ref. [33] and Fig. 1(c), see the mapping between the two in Fig. 2(c) and [38]. Conversely, the FP graph invariant extends naturally to the LC RVdP-like limit ($U = 0, G = 0, \gamma > 0, \kappa_2 > 0$), where an attracting LC adds a S vertex. As Fig. 2(d) shows, this vertex shares the chirality of both the enclos-

ing repellor and the source at infinity, consistent with the Poincaré-Bendixson theorem [37]. Extending the decorated graph invariants to flows with coexisting LCs and FPs, via Fig. 2(d), makes basin adjacency ambiguous: LC “patches” may geometrically enclose other basins rather than border them, a complication detailed in [38]. Figure 2(e) revisits the phase diagram classified according to such FP invariant already producing a rich range of phases. Figure 2(f) illustrates two representative horizontal and vertical cuts of the FP phase diagram in Fig. 2(e), along which the molecule reveals flow structure far beyond the FP classification. Here LCs coexist with FPs, both appearing in attracting and repelling forms.

The flows shown in Fig. 3(a), corresponding to the starred points in Fig. 2(f), reveal the sequence of phase transitions [local (global) bifurcations labelled by ℓ (g)].

$$\bar{\alpha}_1^- S_1^- \xrightarrow{\ell} \bar{\alpha}_2^- S_1^- \xrightarrow{\ell} \bar{\alpha}_2^- S_1^- \bar{S}_2^- \xrightarrow{g} \bar{\alpha}_2^- S_1^- \bar{S}_1^- \xrightarrow{g} \bar{\alpha}_2^- . \quad (5)$$

Starting from the RVdP phase, $\bar{\alpha}_1^- S_1^-$, with a LC and a source (i) a pitchfork bifurcation creates a sink–saddle pair (atom creation $\emptyset \rightarrow V^{(1)} + A_\bullet$), morphing $\bar{\alpha}_1^- S_1^- \rightarrow \bar{\alpha}_2^- S_1^-$. (ii) A subcritical Hopf bifurcation on both repellors nucleates two additional unstable LCs ($A_\circ \rightarrow A_\bullet + \bar{S}^-$) and turns the repellors into attractors, giving $\bar{\alpha}_2^- S_1^- \rightarrow \bar{\alpha}_2^- S_1^- \bar{S}_2^-$. (iii) A (global) homoclinic saddle loop (saddle connecting to itself) forms when a LC expands and collides with the saddle, destroying the cycle and rewiring separatrices; by \mathbb{Z}_2 symmetry ($\hat{a} \rightarrow -\hat{a}$), this produces a new repelling LC immediately after the double homoclinic bifurcation ($V^{(1)} + \bar{S}_2^- \rightarrow V^{(1)} + \bar{S}_1^-$),

leading to $\alpha_2^- S_1^- \bar{S}_1^-$. (iv) Finally, a fold bifurcation of LCs occurs, where two nested cycles of opposite stability mutually annihilate. The annihilation of LCs lets trajectories from the former exterior basin to reach the FP attractors. The result is the bistable KPO phase α_2^- . When varying the Kerr nonlinearity U at fixed G , a similar sequence of transitions arises in the five-FP region, adding more complex transitions, e.g. global heteroclinic bifurcations (saddle to saddle connections); see [38].

Transient signatures of flow-topology transitions: In all four phases, $\bar{\alpha}_1^- S_1^-$, $\bar{\alpha}_2^- S_1^-$, $\alpha_2^- S_1^- \bar{S}_2^-$, and $\alpha_2^- S_1^- \bar{S}_1^-$, $\hat{\rho}_0$ contains a single attracting LC, so the Wigner distributions are essentially equivalent; only the arrangement of saddles, repellors, and repelling LCs differs. These structures leave little trace in the steady state but shape the relaxation pathways. After a quench from the vacuum [Fig. 3(b-e)], the fluctuations expand roughly isotropically in $\bar{\alpha}_1^- S_1^-$ [Fig. 3(b)]. In $\bar{\alpha}_2^- S_1^-$ [Fig. 3(c)] the state is first funneled onto a saddle, then winds around the repellors before settling on the attracting LC. In $\alpha_2^- S_1^- \bar{S}_2^-$ [Fig. 3(d)] it again relaxes to a cycle, but a repelling LC pushes it away from a finite forbidden region. The topological framework uncovers a broader class of nonlocal transitions arising from g bifurcations. A clear example is the passage from the single-cycle phase $\bar{\alpha}_2, S_1^-$ to the coexistence phase $\alpha_2^-, S_1^- \bar{S}_2^-$ in Fig. 3, driven by a subcritical Hopf bifurcation. Here, the forbidden region in $\alpha_2^- S_1^- \bar{S}_2^-$ grows as the repelling and attracting cycles approach their coalescence [Fig. 3(e)].

The molecule detects transitions that the Liouvillian spectrum misses. In particular, the real Liouvillian gap remains open [Fig. 4], even though the steady state shifts from a LC annulus to a bimodal Wigner state (flow-topology transition $(\bar{\alpha}_1^- S_1^- \leftrightarrow \alpha_2^-)$). For example, although $\bar{\alpha}_1^- S_1^-$ and $\bar{\alpha}_2^- S_1^-$ differ through local changes in the flow, the Liouvillian gap remains unchanged because the restructuring happens among unstable states. The associated signatures appear only in the transients and are hard to extract from \mathcal{L} , as the key changes unfold at early times (large $|\text{Re}\{\lambda_i\}|$). Similarly, the birth of repelling LCs between $\bar{\alpha}_2^- S_1^-$ and $\alpha_2^- S_1^- \bar{S}_2^-$ leaves no traces in the gap, but only indirect traces in decaying modes: a level crossing of λ_1 and λ_2 modes in Fig. 4, signalling an inversion of the slowest relaxation pathway (see [38] for a calculation of the crossing point). Crucially, our invariant shows that the emerging stable FPs do not collide with the existing attractor; rather, they are topologically protected by the appearance of repelling LCs, which act as dynamical barriers in phase space. This follows directly from the adjacency structure of the molecule: only adjacent atoms can interact, so sinks can couple only to the saddles bordering them, and LC creation or annihilation is possible only when cycles are nested or next to saddles and therefore adjacent in the invariant. Because global reorganizations of the flow are not accompanied by degeneracies in the Liouvillian (or Jacobian) spectrum, they

leave the Liouvillian gap unchanged and therefore remain invisible at the spectral level.

The physics in Eq. (2) is accessible across several experimental platforms. Nanomechanical systems are a natural playground to realize the dynamical phases presented here and reconstruct the invariant from the flow [34]. Trapped ions offer tunable effective nonlinearities and effective negative damping via laser-driven sidebands [11]. Levitated nanoparticles offer strong, tunable nonlinearities through optical or electrical trapping, and together with parametric two-mode driving, have already produced controlled self-sustained LCs [43, 44]. Polaritonic microcavities constitute another versatile setting: coupled Kerr microresonators exhibit parametric instabilities and LCs dynamics driven by resonant scattering between bonding and antibonding modes [45]. In cold atoms, optically pumped ensembles realize cavity gain in superradiant Raman lasers [46] and atom-cavity systems can also enter self-oscillating regimes where dissipation drives persistent transport [47]. Superconducting circuits leverage Josephson-junction Kerr nonlinearities and qubit-mediated incoherent gain, enabling single-atom lasing and site-resolved engineered baths in circuit lattices [48–50]. In quantum acoustics, qubit-mechanical coupling should enable the same gain mechanism [51].

Outlook: Our framework shows that flow topology transitions reorganize the relaxation pathways of the quantum dynamics. The same structures should also govern rare activation paths between metastable states, suggesting a bridge to predict the topology of quantum activation pathways in non-equilibrium phases [52, 53]. Our construction assumes a phase space compactified into a sphere, where the molecule reduces to satisfy the Poincaré–Hopf theorem: the indices of attractors, repellors, and saddles sum to the Euler characteristic [38]. Extending it to manifolds such as tori or flux-threaded Brillouin zones would modify these constraints and link flow topology with band topology in nonlinear topological photonics [54, 55], enabling new invariants and previously inaccessible classes of dynamical transitions. Ultimately, the sensitivity of relaxation pathways to local and global bifurcations opens the door to applications paralleling those of local bifurcations, including bifurcation-based amplification and sensing [56] and engineered bosonic code architectures operating near critical points [57], while also intersecting with advances in quantum control landscape engineering [58].

We acknowledge funding from the Ramón y Cajal program (RYC2023-043827-I), funded by MICIU/AEI (10.13039/501100011033) and FSE+. J.d.P. also acknowledges support from the Proyectos de Generación de Conocimiento program (Plan Estatal de Investigación Científica y Técnica y de Innovación), grant PID2024-158923NA-I00, funded by MICIU/AEI (10.13039/501100011033) and FEDER, UE.

[1] A. Leuch, L. Papariello, O. Zilberberg, C. L. Degen, R. Chitra, and A. Eichler, *Physical Review Letters* **117**, 214101 (2016).

[2] I. Kovacic, R. Rand, and S. Mohamed Sah, *Applied Mechanics Reviews* **70**, 020802 (2018).

[3] A. Grimm, N. E. Frattini, S. Puri, S. O. Mundhada, S. Touzard, M. Mirrahimi, S. M. Girvin, S. Shankar, and M. H. Devoret, *Nature* **584**, 205 (2020).

[4] A. Eichler and O. Zilberberg, *Classical and Quantum Parametric Phenomena* (Oxford University Press, 2023).

[5] J. Keeling, M. J. Bhaseen, and B. D. Simons, *Phys. Rev. Lett.* **105**, 043001 (2010).

[6] T. E. Lee and H. R. Sadeghpour, *Phys. Rev. Lett.* **111**, 234101 (2013).

[7] N. Lörch, J. Qian, A. Clerk, F. Marquardt, and K. Hammerer, *Physical Review X* **4**, 011015 (2014).

[8] L. Ben Arosh, M. C. Cross, and R. Lifshitz, *Physical Review Research* **3**, 013130 (2021).

[9] P. Kongkhambut, J. Skulte, L. Mathey, J. G. Cosme, A. Hemmerich, and H. Keßler, *Science* **377**, 670 (2022).

[10] T. Kehrer, C. Bruder, and P. Solanki, *Phys. Rev. Lett.* **135**, 063601 (2025).

[11] J. Liu, Q. Wu, J. E. Moore, H. Haeffner, and C. W. Wächtler, *arXiv:2509.18423* (2025), *arXiv:2509.18423* [quant-ph].

[12] J. J. G. Ripoll, *Quantum information and quantum optics with superconducting circuits* (Cambridge University Press, 2022).

[13] H. Ritsch, P. Domokos, F. Brennecke, and T. Esslinger, *Reviews of Modern Physics* **85**, 553 (2013).

[14] D. Leibfried, R. Blatt, C. Monroe, and D. Wineland, *Reviews of Modern Physics* **75**, 281 (2003).

[15] M. Poot and H. S. J. van der Zant, *Physics Reports* **511**, 273 (2012), *arXiv: 1106.2060*.

[16] C. Brif, R. Chakrabarti, and H. Rabitz, *New Journal of Physics* **12**, 075008 (2010).

[17] S. T. Cundiff and J. Ye, *Rev. Mod. Phys.* **75**, 325 (2003).

[18] W. Cai, Y. Ma, W. Wang, C.-L. Zou, and L. Sun, *Fundamental Research* **1**, 50 (2021).

[19] M. J. Hartmann, F. G. S. L. Brandao, and M. B. Plenio, *Laser & Photonics Reviews* **2**, 527 (2008), *arXiv:0808.2557* [quant-ph].

[20] J. Eisert, M. Friesdorf, and C. Gogolin, *Nature Physics* **11**, 124 (2015).

[21] D. A. Abanin, E. Altman, I. Bloch, and M. Serbyn, *Rev. Mod. Phys.* **91**, 021001 (2019).

[22] M. Soriente, T. L. Heugel, K. Omiya, R. Chitra, and O. Zilberberg, *Physical Review Research* **3**, 023100 (2021).

[23] T. Oka and S. Kitamura, *Annual Review of Condensed Matter Physics* **10**, 387 (2019).

[24] F. Minganti, A. Biella, N. Bartolo, and C. Ciuti, *Physical Review A* **98**, 042118 (2018).

[25] T. Haga, *Physical Review B* **110**, 104303 (2024).

[26] E. I. R. Chiacchio, A. Nunnenkamp, and M. Brunelli, *Phys. Rev. Lett.* **131**, 113602 (2023).

[27] J. del Pino, J. Košata, and O. Zilberberg, *Phys. Rev. Res.* **6**, 033180 (2024).

[28] M. Fu, O. Ameye, F. Yang, J. Košata, J. Del Pino, O. Zilberberg, and E. Scheer, *Physical Review Research* **7**, 033127 (2025).

[29] A. A. Oshemkov and V. V. Sharko, *Sbornik: Mathematics* **189**, 1205 (1998).

[30] J.-P. Blaizot and G. Ripka, *Quantum theory of finite systems* (MIT Press, Cambridge, Mass, 1986).

[31] R. Rossignoli and A. M. Kowalski, *Phys. Rev. A* **72**, 032101 (2005).

[32] V. P. Flynn, E. Cobanera, and L. Viola, *New Journal of Physics* **22**, 083004 (2020), *arXiv:2003.03405* [quant-ph].

[33] G. Villa, J. del Pino, V. Dumont, G. Rastelli, M. Michałek, A. Eichler, and O. Zilberberg, *Science Advances* **11**, ead79311 (2025).

[34] V. Dumont, M. Bestler, L. Catalini, G. Margiani, O. Zilberberg, and A. Eichler, *Phys. Rev. Res.* **6**, 043012 (2024).

[35] K. Seibold, G. Villa, J. del Pino, and O. Zilberberg, *arXiv:2508.16486* (2025), *arXiv:2508.16486* [quant-ph].

[36] P. Glendinning, *Stability, instability and chaos: an introduction to the theory of nonlinear differential equations* (Cambridge university press, 1994).

[37] J. Guckenheimer and P. Holmes, *Nonlinear oscillations, dynamical systems, and bifurcations of vector fields*, Vol. 42 (Springer Science & Business Media, 2013).

[38] Supplemental Material, *Supplemental material* (2025), see Supplemental Material for the construction of the invariant, the semiclassical stability analysis, and the bifurcation sequence in the region where five fixed points coexist with limit cycles.

[39] M. Pandey, R. H. Rand, and A. T. Zehnder, *Nonlinear Dynamics* **54**, 3 (2008).

[40] B. Wielinga and G. J. Milburn, *Physical Review A* **48**, 2494 (1993).

[41] M. Mirrahimi, Z. Leghtas, V. V. Albert, S. Touzard, R. J. Schoelkopf, L. Jiang, and M. H. Devoret, *New Journal of Physics* **16**, 045014 (2014).

[42] S. Dutta, S. Zhang, and M. Haque, *Phys. Rev. Lett.* **134**, 050407 (2025).

[43] M. Reisenbauer, H. Rudolph, L. Egyed, K. Hornberger, A. V. Zasedatelev, M. Abuzarli, B. A. Stickler, and U. Delić, *Nature Physics* **20**, 1629 (2024).

[44] V. Liška, T. Zemáneková, P. Jákl, M. Šiler, S. H. Simpson, P. Zemánek, and O. Brzobohatý, *Nature Physics* **20**, 1622 (2024).

[45] N. Carlon Zambon, S. R. K. Rodriguez, A. Lemaître, A. Harouri, L. Le Gratiet, I. Sagnes, P. St-Jean, S. Ravets, A. Amo, and J. Bloch, *Physical Review A* **102**, 023526 (2020).

[46] J. G. Bohnet, Z. Chen, J. M. Weiner, D. Meiser, M. J. Holland, and J. K. Thompson, *Nature* **484**, 78 (2012).

[47] D. Dreon, A. Baumgärtner, X. Li, S. Hertlein, T. Esslinger, and T. Donner, *Nature* **608**, 494 (2022).

[48] O. Astafiev, K. Inomata, A. O. Niskanen, T. Yamamoto, Y. A. Pashkin, Y. Nakamura, and J. S. Tsai, *Nature* **449**, 588 (2007).

[49] B. Du, Q. Guo, S. López, and R. Ma, *Phys. Rev. Res.* **7**, L022038 (2025).

[50] F. Adinolfi, D. Z. Haxell, A. Bruno, L. Michaud, V. H. Kamrul, P. Pandey, and A. Grimm, *arXiv e-prints* (2025), *arXiv:2511.01027* [quant-ph].

[51] Y. Chu, P. Kharel, W. H. Renninger, L. D. Burkhardt, L. Frunzio, P. T. Rakich, and R. J. Schoelkopf, *Science* **358**, 199 (2017).

[52] M. Marthaler and M. I. Dykman, *Physical Review A* **73**, 042108 (2006).

[53] K. Macieszczak, M. u. u. u. u. Gută, I. Lesanovsky, and J. P. Garrahan, *Phys. Rev. Lett.* **116**, 240404 (2016).

[54] D. Smirnova, D. Leykam, Y. Chong, and Y. Kivshar,

Applied Physics Reviews **7**, 021306 (2020).

- [55] A. Szameit and M. C. Rechtsman, *Nature Physics* **20**, 905 (2024).
- [56] R. Vijay, M. H. Devoret, and I. Siddiqi, *Review of Scientific Instruments* **80**, 111101 (2009).
- [57] L. Gravina, F. Minganti, and V. Savona, *PRX Quantum* **4**, 020337 (2023).
- [58] N. Beato, P. Patil, and M. Bukov, *Phys. Rev. X* **15**, 041014 (2025), publisher: American Physical Society.

Supplemental Material: Quantum Dynamical Signatures of Topological Flow Transitions in Limit Cycle Phases

Alejandro S. Gómez

Javier del Pino

Departamento de Física Teórica de la Materia Condensada and Condensed Matter Physics Center (IFIMAC), Universidad Autónoma de Madrid, E-28049 Madrid, Spain

I. STRUCTURAL AND TOPOLOGICAL ASPECTS OF THE SEMICLASSICAL FLOW

A. Structural stability and Morse–Smale character

Structural stability expresses that a continuous dynamical system, governed by a flow, varies smoothly under small perturbations, remaining topologically equivalent to the original one. A structurally stable system retains its qualitative behavior under small perturbations of its parameters: fixed points (FPs) do not change type, limit cycles (LCs) persist (though their positions and periods may shift), and separatrices deform smoothly without altering their connectivity. In two-dimensional systems, this robustness is ensured when the flow satisfies the Morse–Smale conditions. These require that (i) all FPs and periodic orbits are hyperbolic [1], that (ii) only finitely many of them exist, and that (iii) their stable and unstable manifolds intersect transversely [2, 3] [4].

When only FPs are present, these conditions guarantee that the flow decomposes cleanly into basins separated by saddle manifolds, with no recurrent behavior beyond the FPs themselves. With LCs this picture generalizes naturally: hyperbolic cycles act as periodic attractors or repellors. The transversality condition ensures that the stable and unstable manifolds of saddles and cycles do not form tangencies, thereby forbidding chaotic dynamics and guaranteeing that the phase space remains partitioned into well-defined basins of attraction.

In our model, away from the bifurcation lines in the phase diagrams, the semiclassical flow satisfies these Morse–Smale requirements, ensuring structural stabil-

ity throughout each phase and validating the use of a topological invariant to classify them [5].

B. Construction of the molecule invariant

To build the topological invariant, we proceed by decomposing the flow based on its asymptotic behavior [6]. Let v be a structurally stable flow defined on the compactified space $\mathcal{M} \simeq \mathcal{S}^2$. We define an *atom* as an equivalence class of flow-invariant compact regions $N \subset \mathcal{M}$ containing exactly one recurrent set (attractor or repellor) or a connected set of saddle points. There are exactly five atom types: point attractors (A_\bullet) and repellors (A_\circ), attracting (S) and repelling (\bar{S}) LCs, and saddle regions $V^{(n)}$ with complexity n , i.e., containing n saddle points.

To assemble these atoms into the global *molecule* graph: We define a *cutting set* consisting of a disjoint family of neighborhoods: a disc enclosing each FP atom (A_\bullet, A_\circ) for attractor/repellors respectively, an annulus enclosing each LC atom (S, \bar{S}) for attracting/repelling LCs respectively, and a neighborhood $\mathcal{N}(V^{(n)})$ for each saddle complex. Cutting the manifold along the boundaries of these sets isolates the atoms, which become the nodes of the graph. Then, we assign directed edges based on the separatrix flow connecting these boundaries. We distinguish three bond types, s , t and u for connecting repellors to saddles, repellors to attractors and saddles to attractors respectively. Finally, to capture the orientation of the spiraling motion, we assign a local chirality $\sigma \in \{+, -, o\}$ to each atom defined by the local winding relative to the rotating frame frequency [5] (CW +, CCW -) or undefined (o) for overdamped character, extending the classification of Morse–Smale flows [6].

C. Local and global bifurcation rules in molecule invariant

The global topology of the flow is constrained by the Poincaré–Hopf index theorem on the sphere, which requires the sum of the indices of all singularities (FPs) to satisfy $\sum \text{ind}(x_i) = \chi(\mathcal{S}^2) = 2$ [7]. In terms of our atoms: $N_\circ + N_\bullet - N_\times = 2$, where N_\circ , N_\bullet , and N_\times are the numbers of sources, sinks, and saddles, respectively. Note that hyperbolic LCs (S, \bar{S}) carry a Poincaré index of 0, so they can be created or destroyed without altering this sum, although their appearance fundamentally changes the connectivity of the molecule. Local events such as saddle–node bifurcations, supercritical and subcritical Hopf bifurcations, and chirality flips preserve the total index while changing the molecule in controlled ways consistent with these adjacency constraints.

The molecule invariant imposes topological rules on the allowed phase transitions. Because physical bifurcations correspond to specific operations on the graph (such as edge contraction or vertex merging), only atoms that are

adjacent in the molecule can interact. This means that a FP can only undergo a bifurcation with a saddle if they share a direct bond (i.e. separatrix connection), and two LCs can collide and annihilate if they are nested, which is adjacent in the invariant. This structure also provides a mechanism of topological protection: an attractor is dynamically separated by other atoms if they are not adjacent (e.g., a repelling LC acting as a barrier as in Fig 3 in Main Text), ensuring that local and global reorganizations must propagate through the graph neighbor by neighbor rather than jumping between disconnected atoms.

The molecule invariant introduced here can be formally mapped to the colored graph invariants developed for FP flows in driven-dissipative systems [3]. Specifically, the molecule represents a dual graph of the phase-space cutting-set, where each invariant basin of attraction or repulsion is condensed into a single vertex (atom). While the colored graph representation (Fig. 5, top rows) faithfully depicts the geometric arrangement of basins on the sphere, the strict topological constraints governing bifurcations are often obscured by the visual complexity of nested domains. By contrast, the molecule invariant (Fig. 5, bottom rows) explicitly encodes adjacency as graph connectivity, rendering the selection rules for phase transitions.

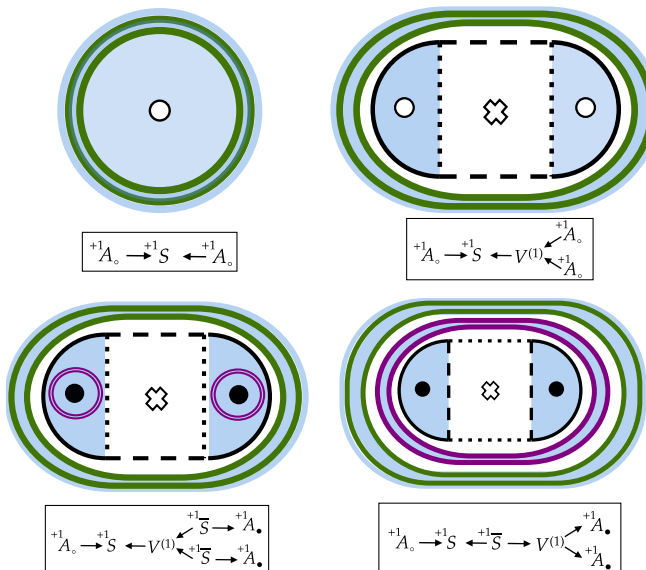


FIG. 5. *Molecule invariant vs graph invariant.* Comparison between the geometric colored graph representation (top), adapted from [3], and the molecule invariant (bottom) for the same phases. The panels correspond to the phases shown in Fig. 3(a) of the main text.

II. LOCAL TRANSITIONS: CRITICAL LINES AND LIOUVILLIAN SPECTRUM

A. Mean field flow: fixed point phase diagram

The dynamics of the system are governed by the Lindblad master equation for the density matrix $\hat{\rho}$:

$$\partial_t \hat{\rho} = -i[\hat{\mathcal{H}}, \hat{\rho}] + \kappa_+ \mathcal{D}[\hat{a}^\dagger] \hat{\rho} + \kappa_- \mathcal{D}[\hat{a}] \hat{\rho} + \kappa_2 \mathcal{D}[\hat{a}^2] \hat{\rho}, \quad (\text{II.1})$$

where the Hamiltonian in the rotating frame is given by

$$\hat{\mathcal{H}} = -\Delta \hat{a}^\dagger \hat{a} + \frac{U}{2} \hat{a}^\dagger^2 \hat{a}^2 + \frac{G}{2} (\hat{a}^\dagger^2 + \hat{a}^2). \quad (\text{II.2})$$

In the limit of large photon numbers, we apply the mean-field approximation, e.g., $\langle \hat{a}^\dagger \hat{a} \hat{a} \rangle \approx |\alpha|^2 \alpha$, where $\alpha \equiv \langle \hat{a} \rangle$. The equation of motion for the complex amplitude α reads:

$$i\dot{\alpha} = \left[-\Delta + i\frac{\gamma}{2} + (U - i\kappa_2) |\alpha|^2 \right] \alpha + G\alpha^*, \quad (\text{II.3})$$

with the effective linear rate $\gamma \equiv \kappa_+ - \kappa_-$. Decomposing the amplitude into real quadratures $\alpha = u + iv$ and defining the intensity $R^2 = u^2 + v^2$, we obtain the planar flow presented in Eq. (3) of the main text:

$$\begin{aligned} \dot{u} &= \left(\frac{\gamma}{2} - \kappa_2 R^2 \right) u - (\Delta + G - UR^2) v, \\ \dot{v} &= \left(\frac{\gamma}{2} - \kappa_2 R^2 \right) v + (\Delta - G - UR^2) u. \end{aligned} \quad (\text{II.4})$$

It is instructive to express the dynamics in polar coordinates $\alpha = re^{i\phi}$, which yields:

$$\dot{r} = r \left(\frac{\gamma}{2} - \kappa_2 r^2 - G \sin(2\phi) \right), \quad (\text{II.5a})$$

$$\dot{\phi} = \Delta - Ur^2 - G \cos(2\phi). \quad (\text{II.5b})$$

Note that the angular equation is valid for $r \neq 0$, while the origin $r = 0$ is a singular point of the polar map but a well-defined FP of the Cartesian flow.

The FPs (r_*, ϕ_*) obey $\dot{r} = \dot{\phi} = 0$. The origin $r_* = 0$ (or $\alpha = 0$) is a trivial solution for all parameter values. Due to the \mathbb{Z}_2 symmetry of the Liouvillian under the parity transformation $\hat{a} \rightarrow -\hat{a}$, nontrivial FPs appear in pairs (r_*, ϕ_*) and $(r_*, \phi_* + \pi)$, corresponding to $\pm \alpha_*$. Consequently, the total number of FPs is always odd. For nontrivial solutions $(r_* > 0)$, the stationarity conditions imply:

$$G \sin(2\phi_*) = \frac{\gamma}{2} - \kappa_2 r_*^2, \quad G \cos(2\phi_*) = \Delta - Ur_*^2. \quad (\text{II.6})$$

Squaring and summing these equations eliminates the phase ϕ_* , leading to a self-consistency condition for the intensity $I_* \equiv r_*^2$:

$$G^2 = \left(\frac{\gamma}{2} - \kappa_2 I_* \right)^2 + (\Delta - UI_*)^2. \quad (\text{II.7})$$

This can be rearranged into a quadratic equation for the intensity, $SI_\star^2 - AI_\star + C = 0$, with coefficients defined as [8]:

$$S \equiv \kappa_2^2 + U^2, \quad A \equiv 2\Delta U + \gamma\kappa_2, \quad C \equiv \frac{\gamma^2}{4} + \Delta^2 - G^2. \quad (\text{II.8})$$

The solutions are formally given by:

$$I_{\star,\pm} = \frac{A \pm \sqrt{\mathcal{D}}}{2S}, \quad \text{with } \mathcal{D} = 4SG^2 - B^2, \quad (\text{II.9})$$

where we have introduced the auxiliary parameter $B \equiv U\gamma - 2\kappa_2\Delta$ and a discriminant $\mathcal{D} = A^2 - 4SC$ [9, 10].

Physical FPs correspond to real, positive intensities $I_\star > 0$. We classify the solutions based on the drive strength G and the sign of A in Eq. (II.8). We define two critical drive amplitudes, namely [11]

$$G_{\min} \equiv \frac{|B|}{2\sqrt{S}}, \quad G_\star \equiv \frac{\sqrt{A^2 + B^2}}{2\sqrt{S}}. \quad (\text{II.10})$$

Here, G_{\min} corresponds to the threshold where the discriminant becomes non-negative ($\mathcal{D} \geq 0$), and G_\star corresponds to the point where one solution branch crosses zero ($C = 0$). The FP landscape is divided into three distinct regions:

1. **Single Trivial Attractor (1 FP):** For $|G| < G_{\min}$,

$$J(u, v) = \begin{pmatrix} \frac{\gamma}{2} - \kappa_2(r^2 + 2u^2) + 2Uuv & -(\Delta + G) + Ur^2 + 2Uv^2 - 2\kappa_2uv \\ \Delta - G - Ur^2 - 2Uu^2 - 2\kappa_2uv & \frac{\gamma}{2} - \kappa_2(r^2 + 2v^2) - 2Uuv \end{pmatrix}. \quad (\text{II.11})$$

The stability analysis follows the standard trace-determinant plane [8], where the trace $\mathfrak{T} \equiv \text{tr}(J)$ and determinant $\mathfrak{D} \equiv \det(J)$, read

$$\mathfrak{T}(r^2) = \gamma - 4\kappa_2r^2, \quad (\text{II.12})$$

$$\mathfrak{D}(r^2) = r^2(4Sr^2 - 2A), \quad (\text{II.13})$$

with S and A defined in Eq. (II.8). The character of the FP depends on the Jacobian discriminant $\delta_J \equiv \mathfrak{T}^2 - 4\mathfrak{D}$:

$$\delta_J(r^2) = \gamma^2 + 16Ur^2(\Delta - Ur^2). \quad (\text{II.14})$$

Substituting the explicit solutions (II.9) into Eq. (II.12) simplifies to

$$\mathfrak{D}(I_{\star,\pm}) = 2I_{\star,\pm}(2SI_{\star,\pm} - A) = \pm 2I_{\star,\pm}\sqrt{\mathcal{D}}. \quad (\text{II.15})$$

Since physical FPs require $I_\star > 0$ and the existence discriminant $\mathcal{D} \geq 0$, the sign of the determinant is fixed

no real nontrivial solution exists; only the trivial fixed point remains.

2. **Five-Solution Region (5 FPs):** This phase requires two distinct positive roots $I_{\star,\pm} > 0$, which occurs when $A > 0$ and $C > 0$ (i.e., $|G| < G_\star$). For $A > 0$ and $G_{\min} < |G| < G_\star$, the system supports five FPs: the origin and two nontrivial pairs.

3. **Three-Solution Region (3 FPs):** This phase occurs when exactly one root $I_\star > 0$. For $A > 0$, this requires a negative product of roots ($|G| \geq G_\star$). For $A < 0$, a real discriminant and a positive root likewise require a negative product, again giving $|G| \geq G_\star$. Thus, for any A , the condition $|G| \geq G_\star$ yields exactly three FPs: the origin and one nontrivial pair.

These analytic bounds G_{\min} and G_\star in Eq. (II.10) thus define the transition lines (bifurcations) observed in the phase diagrams of Fig. 2 in the main text. Specifically, G_{\min} marks the saddle-node bifurcation creating the 5-FP region, while G_\star marks the supercritical pitchfork bifurcation where the origin loses stability.

B. Linear stability analysis and Jacobian

The stability is governed by the Jacobian matrix of the flow in Eq. (II.4), $J(\mathbf{r}) \equiv \partial(f_u, f_v)/\partial(u, v)$. Differentiating the flow equations, the Jacobian evaluated at a point with intensity $R^2 = r^2$ is

$$J(u, v) = \begin{pmatrix} \frac{\gamma}{2} - \kappa_2(r^2 + 2u^2) + 2Uuv & -(\Delta + G) + Ur^2 + 2Uv^2 - 2\kappa_2uv \\ \Delta - G - Ur^2 - 2Uu^2 - 2\kappa_2uv & \frac{\gamma}{2} - \kappa_2(r^2 + 2v^2) - 2Uuv \end{pmatrix}. \quad (\text{II.11})$$

solely by the solution branch:

$$\mathfrak{D}(I_{\star,+}) > 0, \quad \mathfrak{D}(I_{\star,-}) < 0. \quad (\text{II.16})$$

The “-” branch (when it exists physically) contains only saddle points. The “+” branch is always an antisaddle (sink or source), and its stability is determined solely by the trace \mathfrak{T} .

Hopf Bifurcation: The Hopf instability occurs when the trace vanishes, $\mathfrak{T}(I_{\star,+}) = 0$. This requires $4\kappa_2 I_{\star,+} = \gamma$. Solving for G yields the critical Hopf drive:

$$G_H = \frac{1}{2\sqrt{S}} \sqrt{B^2 + \left(\frac{S\gamma}{2\kappa_2} - A \right)^2}. \quad (\text{II.17})$$

At $|G| = G_H$, the system undergoes a subcritical Hopf bifurcation, giving rise to an unstable LCs.

Node-Focus Transition: The transition from monotonic (node) to oscillatory (focus) approach to the FP occurs

when $\delta_J(I_{\star,+}) = 0$. Solving this condition leads to the threshold:

$$G_F^{(\pm)} = \frac{1}{2\sqrt{S}} \sqrt{B^2 + \left[\frac{S}{2U} \left(2\Delta \pm \sqrt{\gamma^2 + 4\Delta^2} \right) - A \right]^2}, \quad (\text{II.18})$$

which also manifest a level crossing of Liouvillian eigenmodes in main text Fig. 4. For $U = 0, \kappa_2 \neq 0$ (2DPO), $\delta_J = \gamma^2 > 0$, implying the FP is always a node.

Stability of the Origin: Linearizing around the trivial solution $\alpha = 0$ ($r = 0$), the eigenvalues are

$$\varepsilon_{\pm} = \gamma/2 \pm \sqrt{G^2 - \Delta^2}. \quad (\text{II.19})$$

We distinguish two regimes split by a second order exceptional point (EP) at $G = \Delta$:

- $|G| < |\Delta|$: The eigenvalues are complex conjugates, $\varepsilon_{\pm} = \gamma/2 \pm i\Omega$. The origin is a stable focus if $\gamma < 0$ (loss dominates gain) and unstable source if $\gamma > 0$.
- $|G| > |\Delta|$: The eigenvalues become real. If $|\gamma| > 2\sqrt{G^2 - \Delta^2}$, the origin remains a node (stable if $\gamma < 0$). Else, if $|\gamma| < 2\sqrt{G^2 - \Delta^2}$, one eigenvalue becomes positive, turning the origin into a saddle point (pitchfork bifurcation).

C. Gap closings, oscillating-mode gap, and global flow-topology changes

Each eigenvalue λ_j of the Liouvillian $\tilde{\mathcal{L}}$ (main text Eq. (1)) has a real part $\text{Re}\{\lambda_j\} < 0$ that sets the decay rate of a transient mode and an imaginary part $\text{Im}\{\lambda_j\}$ that determines its oscillation frequency. Stationary states correspond to modes with $\text{Re}\{\lambda_j\} = 0$, and in the case of LCs they may carry nonzero $\text{Im}\{\lambda_j\}$, reflecting persistent oscillations and the spontaneous breaking of continuous time-translation symmetry. [9, 10]

Closing the *Liouvillian gap*, i.e. defined as the smallest nonzero decay rate,

$$\Delta_L = \min_{i \neq 0} [-\text{Re}\{\lambda_i\}], \quad (\text{II.20})$$

signals critical slowing down and a sharp transition in $\hat{\rho}_0$: relaxation toward the steady state becomes arbitrarily slow as the dominant decay mode vanishes. However, dynamical phase transitions can also occur in the transient regime without closing Δ_L . This is captured by the so called oscillating-mode gap [11], defined from the least-damped oscillatory modes:

$$\Delta_{\text{OM}} = \min_{i: \text{Im}\{\lambda_i\} \neq 0} [-\text{Re}\{\lambda_i\}]. \quad (\text{II.21})$$

This quantity is sensitive to EPs in the Liouvillian excitation spectrum [12]. At a chirality-loss transition (such as the DPO \rightarrow KPO crossover), two complex eigenvalues cross on the real axis. Physically, this marks a sharp

transition from underdamped (spiraling relaxation) to overdamped decay. Across this transition Δ_{OM} varies, while Δ_L remains open.

Global flow-topology changes, instead, reroute relaxation trajectories (e.g. due to LC-LC annihilation) without modifying the low-lying Liouvillian spectrum. Both Δ_L and Δ_{OM} remain essentially unchanged, while the transient Wigner dynamics reorganize abruptly. Figure 3 of the main text illustrates this mismatch, showing clear dynamical transitions in the time-dependent Wigner function that are invisible to the Liouvillian gaps.

D. Exceptional point and chirality loss in fixed-point phases

Figure 1(b) in the main text highlights a key point: two stationary phases can look essentially identical at the level of the steady state, yet differ in their underlying mean-field dynamics. In both cases, the semiclassical flow features two attractors separated by a saddle, producing a bimodal Wigner function. However, the corresponding phase-space flows (see main text Fig. 1(d)) are topologically inequivalent, with signatures in the Jacobian fluctuation spectrum and in the mapping between Liouvillian spectra shown in main text Fig. 1(c), as discussed below.

In the FP phases associated with the KPO/DPO

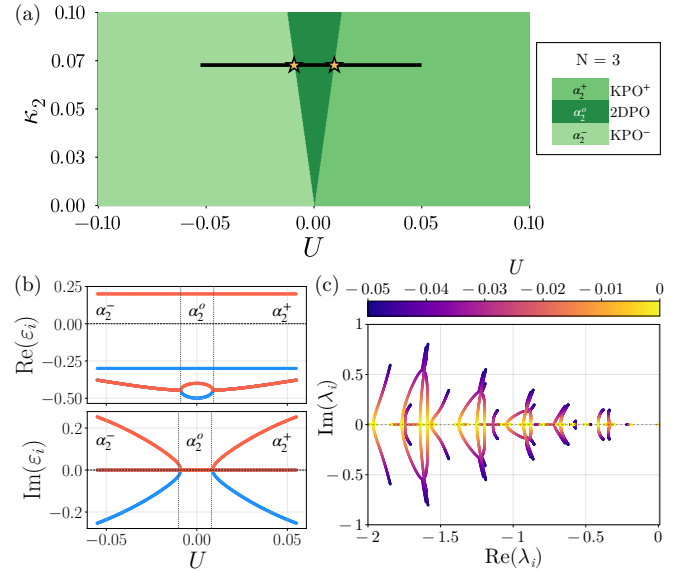


FIG. 6. *Chirality loss transition.* (a) Phase diagram in the (U, κ_2) plane showing the transition between the chiral (underdamped) KPO (α_2^{\pm}) and the achiral (overdamped) 2DPO (α^o) phases. Stars mark the exceptional points along the $\kappa_2 = 0.07$ cut line. (b) Real and imaginary parts of the Jacobian eigenvalues ε_i along the cut, showing the coalescence of eigenvalues in the overdamped region. (c) Evolution of the Liouvillian spectrum λ_i across the transition (from $U = -0.05$ to 0), where oscillating modes (darker colors) collapse onto the real axis (lighter colors).

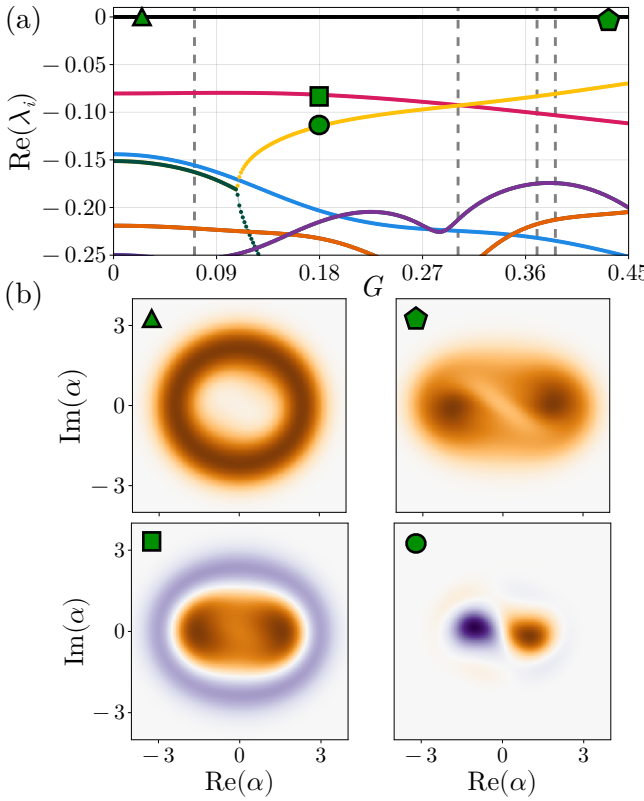


FIG. 7. *Liouvillian spectrum and low-lying decay eigenmodes.* (a) Real part of the Liouvillian eigenvalues as in Fig4 in the main text. (b) Wigner function of the eigenmodes 0, 1 and 2 marked with symbols in (a)

crossover (cf. phase diagram at Fig. 6(a)), the chirality-loss transition $3\alpha_2^- \rightarrow 3\alpha_2^o$ corresponds to an exceptional point of the Jacobian governing fluctuations around the attractor. An explicit analysis of the Jacobian eigenvalues as functions of κ_2/U and G/γ , at zero detuning $\Delta = 0$, leads to the EP condition in Eq. (II.18), namely

$$\frac{\kappa_2}{U} = 2 \pm \sqrt{16 \left(\frac{G}{\gamma} \right)^2 - 1}, \quad (\text{II.22})$$

where the Jacobian eigenspectrum coalesces, as noted in the eigenvalues in Fig. 6(b) and corresponding eigenvectors (not shown). At this line, the dynamics undergoes a transition from underdamped (finite chirality / symplectic norm) to overdamped (zero chirality) behavior. This change is reflected in the oscillating-mode gap of the Liouvillian but does not close the steady-state gap, see Fig. 6(c).

E. Hopf bifurcation and onset of the Rayleigh–Van der Pol LC

In the Rayleigh–Van der Pol (RVdP) limit, linearizing the Liouvillian around the trivial steady state reveals a Hopf instability: a conjugate pair of eigenvalues crosses the imaginary axis, which can be obtained from the Jacobian analysis [10]. At this point, the real part of the leading decay mode vanishes, the Liouvillian gap closes, and the system develops a finite oscillation frequency set by the imaginary part of this pair, in agreement with the RVdP behavior shown in Fig. 1 of the main text.

For the sequence of phases with LCs in Fig. 3(a) of the main text, the critical drive G_H given by Eq. (II.17) instead marks an inversion of the slowest relaxation pathway. It is obtained by evaluating the Jacobian at the relevant fixed point and relating its eigenvalues to the low-lying Liouvillian modes λ_1 and λ_2 . Requiring their decay rates to coincide yields the analytic expression quoted in the main text. Figure 7(a,b) compares this prediction with numerical spectra, showing the level crossing of $\text{Re}\{\lambda_{1,2}\}$ at G_H .

III. GLOBAL BIFURCATIONS AND THE 5 FP REGION

A. Detection of global attractors and bifurcations

To identify and characterize LCs within the semiclassical vector flow, we numerically integrate the equations (II.4) using DifferentialEquations.jl [13]. Since attracting and repelling LCs act as hyperbolic sets, they can be detected by forward- and backward-integrating trajectories initialized in appropriate basins of attraction. We prioritize search regions that contain unstable FPs whose indices imply the necessity of an enclosing attracting boundary to satisfy the Poincaré–Hopf theorem. The flow is evolved for a sufficiently long time to ensure the decay of transient dynamics. We then isolate the asymptotic tail of the trajectory by discarding the initial segment. A LC is identified if the remaining trajectory satisfies the convergence condition $|r(t + T^*) - r(t)| < \epsilon$, with $\epsilon \ll 1$, where T^* is the unknown LC period.

B. Global phases and bifurcations in the 5 FP region

We proceed to analyze the sequence of topological transitions observed as the ratio U/γ is varied, which reveals a rich interplay between local instabilities and global reorganizations of the phase space. Starting from a self-oscillatory phase characterized by a single unstable source surrounded by an attracting LC, the system first undergoes a double Saddle-Node on Invariant Circle (SNIC) bifurcation $\bar{\alpha}_1^- S_1^- \mapsto \alpha_2^+ \bar{\alpha}_1^o$ Fig. 8(a)-(b). In this global event, two pairs of saddle-node FPs nucleate directly upon the invariant circle of the LC. Unlike a standard local bifurcation, the SNIC destroys the periodic orbit not by reducing its amplitude to zero, but by diverging its period as the flow becomes arrested at the emerging stable nodes.

As the parameter is increased further, the global manifolds of the newly created saddles undergo a heteroclinic reconnection $\alpha_2^+ \bar{\alpha}_1^o \mapsto \alpha_2^+ \bar{\alpha}_1^o S_1^+$ Fig. 8(b)-(c). The unstable manifolds of the saddles, which initially terminated at the local sinks, reconnect with the stable manifolds of their symmetric counterparts. This global rewiring births a large, enclosing attracting LC that surrounds the entire fixed-point complex, marking the onset of a phase where local stationarity coexists with large-amplitude oscillatory capabilities.

The internal structure of this coexistence phase subsequently evolves through homoclinic bifurcations $\alpha_2^+ \bar{\alpha}_1^o S_1^+ \mapsto \alpha_2^+ \bar{\alpha}_1^o S_1^+ \bar{S}_2^-$ Fig. 8(c)-(d). Here, the stable separatrix of each saddle contracts and collides with the saddle itself. This collision generates a repelling LC surrounding each local sink, effectively creating a dynamical barrier that isolates the basin of attraction of the FPs from the outer flow. These repelling cycles, as the nonlinearity evolves, shrink and eventually collapse onto the stable nodes in a subcritical Hopf bifurcation $\alpha_2^+ \bar{\alpha}_1^o S_1^+ \bar{S}_2^- \mapsto \bar{\alpha}_2^+ \bar{\alpha}_1^o S_1^+$ Fig. 8(d)-(e). This event transfers the instability to the FPs, converting the sinks into unstable sources and destroying the repelling cycles.

Finally, the remaining complex of unstable FPs—now consisting of sources and saddles—is annihilated via an inverse saddle-node bifurcation $\bar{\alpha}_2^+ \bar{\alpha}_1^o S_1^+ \mapsto \bar{\alpha}_2^o S_1^+$ Fig. 8(e)-(f). The disappearance of these critical points removes the obstruction to the central flow, allowing trajectories to spiral outwards once more towards the large attracting LC.

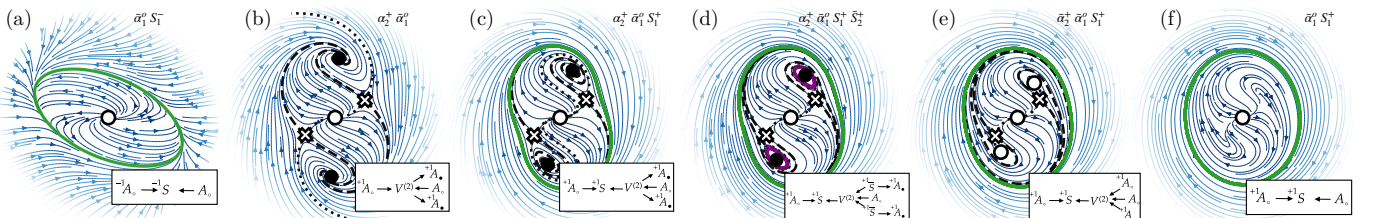


FIG. 8. *Semiclassical flows for phases with 5 FPs.* (a-f) Mean-field vector flows in the (u, v) plane corresponding to the sequence of topological transitions driven by the Kerr nonlinearity $U/\gamma \in \{0.01, 0.2, 0.28, 0.32, 0.4, 0.6\}$ at fixed two-photon drive amplitude $G/\gamma = 0.4$ (other parameters as in Fig 2 of the main text). Green (purple) closed curves denote attracting (repelling) LCs S (\bar{S}), black (white) dots represent point attractors (repellors) and dashed (dotted) lines indicate the stable (unstable) manifolds of the saddle points (crosses).

- [1] In this context, hyperbolicity ensures the dynamics are decisive: at any equilibrium or closed loop, the system strictly attracts or repels nearby trajectories, with no neutral directions where behavior is ambiguous.
- [2] M. Peixoto, *Topology* **1**, 101 (1962).
- [3] G. Villa, J. del Pino, V. Dumont, G. Rastelli, M. Michalek, A. Eichler, and O. Zilberberg, *Science Advances* **11**, eadtk9311 (2025).
- [4] The stable (unstable) manifold is the set of all trajectories winding into (out of) a FP or cycle. Transversality requires that if these manifolds intersect, their tangent vectors at the intersection point must span the entire phase space; visually, they must cross at a non-zero angle rather than

- sharing a common tangent.
- [5] M. Soriente, T. L. Heugel, K. Omiya, R. Chitra, and O. Zilberberg, *Physical Review Research* **3**, 023100 (2021).
- [6] A. A. Oshemkov and V. V. Sharko, *Sbornik: Mathematics* **189**, 1205 (1998).
- [7] M. Nakahara, *Geometry, topology and physics* (CRC press, 2018).
- [8] R. H. Rand, *Lecture notes on nonlinear vibrations* (2012).
- [9] F. Minganti, A. Biella, N. Bartolo, and C. Ciuti, *Physical Review A* **98**, 042118 (2018).
- [10] S. Dutta, S. Zhang, and M. Haque, *Phys. Rev. Lett.* **134**, 050407 (2025).
- [11] T. Haga, *Physical Review B* **110**, 104303 (2024).
- [12] F. Minganti, A. Miranowicz, R. W. Chhajlany, and F. Nori, *Physical Review A* **100**, 062131 (2019).
- [13] C. Rackauckas and Q. Nie, *Journal of Open Research Software* **5** (2017).